

The brightest X-ray AGNs at redshift $3 \lesssim z \lesssim 6$

Cameron Heather,^{1*} Teeraparb Chantavat,² Siri Chongchitnan,¹ and Poemwai Chainakun^{3,4}

¹Warwick Mathematics Institute, University of Warwick, Zeeman Building, Coventry CV4 7AL, UK

²Institute for Fundamental Study, Naresuan University, Phitsanulok 65000, Thailand

³School of Physics, Institute of Science, Suranaree University of Technology, Nakhon Ratchasima 30000, Thailand

⁴Centre of Excellence in High Energy Physics and Astrophysics, Suranaree University of Technology, Nakhon Ratchasima 30000, Thailand

Accepted XXX. Received YYY; in original form ZZZ

ABSTRACT

Given recent X-ray observations of high-redshift active galactic nuclei (AGNs), we consider whether the extreme luminosities of these AGNs are consistent with current semi-analytical models. In particular, we apply extreme-value statistics (EVS) to obtain predictions of extreme X-ray luminosities of AGNs in the redshift range $3 \lesssim z \lesssim 6$. We apply this formalism using different X-ray luminosity functions and compare the predicted extreme luminosities to AGNs in the Stripe-82 X-ray catalogue. We find a general consistency between data and the EVS predictions although there is some tension with certain luminosity functions. In addition, the extreme X-ray luminosities are found to be at least an order of magnitude below the Eddington luminosity limit. We discuss possible extensions to this model, including extrapolating our results to even higher redshifts ($z \gtrsim 10$) where AGNs have recently been observed.

Key words: Galaxies: nuclei, statistics. X-ray: galaxies.

1 INTRODUCTION

Active Galactic Nuclei (AGNs) are some of the most energetic astrophysical objects in the Universe. They are created by the accretion of matter onto supermassive black holes (SMBHs) with typical masses of $M_{\text{BH}} \sim 10^5\text{--}10^9 M_{\odot}$ at their cores (Rees 1984; Fabian 2012; Yuan & Narayan 2014; Netzer 2015; Inayoshi et al. 2020). Among the various wavelengths used to study AGNs, X-ray observations provide a unique window into the innermost regions closest to the event horizon of the black hole.

During the accretion process, the gravitational energy of the infalling gas is converted into radiation, primarily in the form of optical and UV photons. These photons are Compton up-scattered by high-energy electrons within the corona, producing a continuum of X-ray emission whose spectrum is characterized by a power-law shape with a photon index Γ and a cut-off energy E_{cut} (Pozdnyakov et al. 1983; Rybicki & Lightman 1986; Mushotzky et al. 1993). The AGN coronal temperature is controlled by annihilation and pair production through heating and cooling processes (e.g. Fabian et al. 2015).

The most luminous AGNs, with X-ray luminosity L_X as large as $10^{45} \text{ erg s}^{-1}$, stand out as extraordinary laboratories for understanding extreme astrophysical processes (e.g. Stanley et al. 2017; Veronesi et al. 2023). Their immense luminosities result from the highly efficient energy conversion in the accretion process, making them critical probes of the interplay between SMBHs and their extreme environments.

Examining the most luminous AGNs is essential for many reasons: Their exceptional brightness enables their detection across immense cosmic distances, serving as crucial markers for investigating the

high-redshift Universe (Aird et al. 2015). These AGNs also act as indicators for the growth of SMBHs and galaxy evolution, spanning the epoch of reionization and beyond. Understanding how such luminous AGNs form and evolve provides insight into the co-evolution of SMBHs and their host galaxies (Kormendy & Ho 2013). Furthermore, the extreme physical conditions within the luminous AGNs test the limits of the theoretical models. Their high accretion rates, intense radiation, and strong outflows are valuable tests of our understanding of accretion physics, radiation processes, and feedback mechanisms at extreme energies (Fabian 2012).

The most luminous AGNs also play a pivotal role in shaping their cosmic environments. Their energetic feedback can regulate star formation in their host galaxies through powerful winds and jets, profoundly influencing galaxy evolution (Sijacki et al. 2007; Booth & Schaye 2009). At the largest scales, these AGNs impact the intergalactic medium, contributing to heating and metal enrichment (Fabjan et al. 2010). By studying the most luminous AGNs, we gain a better understanding of the mechanisms by which energy is redistributed across scales, connecting SMBHs to other larger-scale structures.

In this work, we will study the abundance and brightness of the most luminous X-ray AGNs using extreme-value statistics (EVS). This framework has previously been applied to estimate the abundances of the most massive Pop III stars (Chantavat et al. 2023), the most massive galaxy clusters (Chongchitnan & Silk 2012), extreme primordial black holes (Chongchitnan et al. 2021; Chongchitnan & Silk 2021), and most recently, the brightest *JWST* galaxies at $z \gtrsim 9$ (Heather et al. 2024).

Our EVS modelling will allow us to test various semi-analytical models of the X-ray luminosity functions by comparing their predictions of extreme X-ray luminosities against data from the *Stripe 82*

* E-mail: cameron.heather@warwick.ac.uk

X-ray catalogue, a benchmark dataset for X-ray surveys combining data from the *Chandra* and *XMM-Newton* space telescopes (LaMassa et al. 2013, 2016, 2024). In particular, we will use the so-called *S82-XL* data from Pecca et al. (2024) and LaMassa et al. (2024), and focus on AGNs at redshifts $3 \lesssim z \lesssim 6$. The central goal of this work is to quantify the consistency (or tension) between theory and observation.

The rest of this paper is organized as follows. In Section 2, we present a survey of models of the X-ray luminosity functions and their associated observables. Section 4 details our EVS modelling, with the main results (the predictions of extreme AGN luminosities across redshifts) shown in Section 5. We discuss the implications of our findings in Section 6.

We will assume a flat Λ CDM cosmology with $H_0 = 70 \text{ km s}^{-1} \text{ Mpc}^{-1}$, $\Omega_m = 0.3$ and $\Omega_\Lambda = 0.7$. We work in natural units with $c = 1$.

2 THE X-RAY LUMINOSITY FUNCTION

The X-ray luminosity function, $d\Phi/d \log L_X$, refers to the differential AGN number density, Φ , per logarithmic interval in X-ray luminosity L_X . In the literature, the luminosity function is often modelled as a double power-law function (Maccacaro et al. 1983, 1991)

$$\frac{d\Phi(L_X, z=0)}{d \log L_X} = A \left[\left(\frac{L_X}{L_*} \right)^{\gamma_1} + \left(\frac{L_X}{L_*} \right)^{\gamma_2} \right]^{-1}, \quad (1)$$

where A is a normalisation factor, L_* is the characteristic luminosity break, and γ_1 and γ_2 describe the slopes of the two power laws.

To model the redshift-dependence of the luminosity function, an evolution factor, $e(z)$, is introduced, so that the X-ray luminosity function becomes

$$\frac{d\Phi(L_X, z)}{d \log L_X} = \frac{d\Phi(L_X, z=0)}{d \log L_X} e(z). \quad (2)$$

In this section, we explore two forms of $e(z)$, namely the *pure density evolution* (PDE) model and the *luminosity-dependent density evolution* (LDDE) model. We also examine a form of the LDDE model with a cut-off redshift value. Fig. 1 gives a graphical summary of the various luminosity functions explored in this section.

2.1 Pure density evolution (PDE) model

This model uses the redshift evolution factor of the form (Hasinger 1998)

$$e(z) = \left(\frac{1+z}{1+z_c} \right)^{p_{\text{den}}}. \quad (3)$$

Fitting this to AGN data at redshifts 3–6, Pouliaxis et al. (2024) gave the value $p_{\text{den}} = -7.35^{+0.39}_{-0.42}$ with $z_c = 3$. Assuming the PDE model, the parameter values in the luminosity function equation (1) are $\log(A/\text{Mpc}^{-3}) = -4.28^{+0.09}_{-0.09}$, $\log(L_*/\text{erg s}^{-1}) = 44.52^{+0.07}_{-0.07}$, $\gamma_1 = 0.21^{+0.08}_{-0.10}$, and $\gamma_2 = 2.23^{+0.14}_{-0.13}$.

2.2 Luminosity-dependent density evolution (LDDE) model

A generalisation of the PDE model proposed by Miyaji et al. (2000) is the luminosity-dependent density model where

$$e(z, L_X) = \left(\frac{1+z}{1+z_c} \right)^{p_{\text{den}} + \beta (\log L_X - 44)}. \quad (4)$$

We will consider various parametrisations of this form given in Pouliaxis et al. (2024), Georgakakis et al. (2015) and Vito et al.

Parameters	Pouliaxis	Georgakakis	Vito
$\log(A/\text{Mpc}^{-3})$	$-4.28^{+0.09}_{-0.10}$	$-4.79^{+0.14}_{-0.17}$	$-4.98^{+0.04}_{-0.04}$
$\log(L_*/\text{erg s}^{-1})$	$44.52^{+0.07}_{-0.07}$	$44.31^{+0.13}_{-0.11}$	$44.72^{+0.09}_{-0.11}$
γ_1	$0.29^{+0.08}_{-0.10}$	$0.21^{+0.15}_{-0.13}$	$0.28^{+0.16}_{-0.19}$
γ_2	$2.38^{+0.15}_{-0.14}$	$2.15^{+0.24}_{-0.21}$	$3.87^{+1.08}_{-0.88}$
p_{den}	$-8.53^{+0.58}_{-0.65}$	$-7.46^{+1.03}_{-1.12}$	$-6.43^{+1.12}_{-1.17}$
β	$2.18^{+0.79}_{-0.81}$	$2.30^{+1.60}_{-1.53}$	$1.18^{+2.06}_{-2.00}$

Table 1. Parameters for the LDDE model of the X-ray luminosity function, with values from Pouliaxis et al. (2024), Georgakakis et al. (2015) and Vito et al. (2014).

(2014). The associated parameter values from these references are shown in Table 1.

2.3 LDDE model with redshift cut-off

This is a model with a more complicated evolution factor of the form (Ueda et al. 2014)

$$e(z, L_X) = \begin{cases} (1+z)^{p_1} & [z \leq z_{c_1}(L_X)] \\ (1+z_{c_1})^{p_1} \left(\frac{1+z}{1+z_{c_1}} \right)^{p_2} & [z_{c_1}(L_X) < z \leq z_{c_2}] \\ (1+z_{c_1})^{p_1} \left(\frac{1+z}{1+z_{c_1}} \right)^{p_2} \left(\frac{1+z}{1+z_{c_2}} \right)^{p_3} & [z > z_{c_2}], \end{cases} \quad (5)$$

where $p_2 = -1.5$, $p_3 = -6.2$ and p_1 is given by the following function of luminosity

$$p_1(L_X) = p_1^* + \beta_1 \log(L_X/44), \quad (6)$$

with $p_1^* = 4.78^{+0.16}_{-0.16}$, $\beta_1 = 0.84^{+0.18}_{-0.18}$. Assuming this model, the parameter values in the luminosity function equation (1) are $\log(A/\text{Mpc}^{-3}) = -5.536^{+0.01}_{-0.01}$, $\log(L_*/\text{erg s}^{-1}) = 43.97^{+0.06}_{-0.06}$, $\gamma_1 = 0.09^{+0.04}_{-0.04}$, $\gamma_2 = 2.71^{+0.09}_{-0.09}$.

The redshift breaks z_{c_1} and z_{c_2} are themselves functions of luminosity, given by a power-law with cut-offs:

$$z_{c_1}(L_X) = \begin{cases} z_{c_1}^* (L_X/L_{a_1})^{\alpha_1} & [L_X \leq L_{a_1}] \\ z_{c_1}^* & [L_X > L_{a_1}], \end{cases} \quad (7)$$

and

$$z_{c_2}(L_X) = \begin{cases} z_{c_2}^* (L_X/L_{a_2})^{\alpha_2} & [L_X \leq L_{a_2}] \\ z_{c_2}^* & [L_X > L_{a_2}]. \end{cases} \quad (8)$$

The parameters values are given in Ueda et al. (2014). We list them here for completeness:

$$z_{c_1}^* = 1.86^{+0.07}_{-0.07}, \log(L_{a_1}/\text{erg s}^{-1}) = 44.61^{+0.07}_{-0.07}, \alpha_1 = 0.29^{+0.02}_{-0.02} \\ z_{c_2}^* = 3, \log(L_{a_2}/\text{erg s}^{-1}) = 44, \alpha_2 = -0.1.$$

Fig. 1 shows the various luminosity functions at three redshift values, $z = 3, 4.5$ and 6. We choose to work with the central values for the parameters given, since the errors provided are mostly small and would minimally affect the EVS results in Section 4.

In Fig. 1, we see that the luminosity functions are generally of the same double-power law shape with similar magnitudes. However, at the high luminosity end, the Vito model decreases most steeply, predicting the least number of the brightest AGNs. We also note that as redshift increases, the low luminosity end shows increasing disparity amongst the models, with the Ueda model dominating above other models at $z \approx 6$.

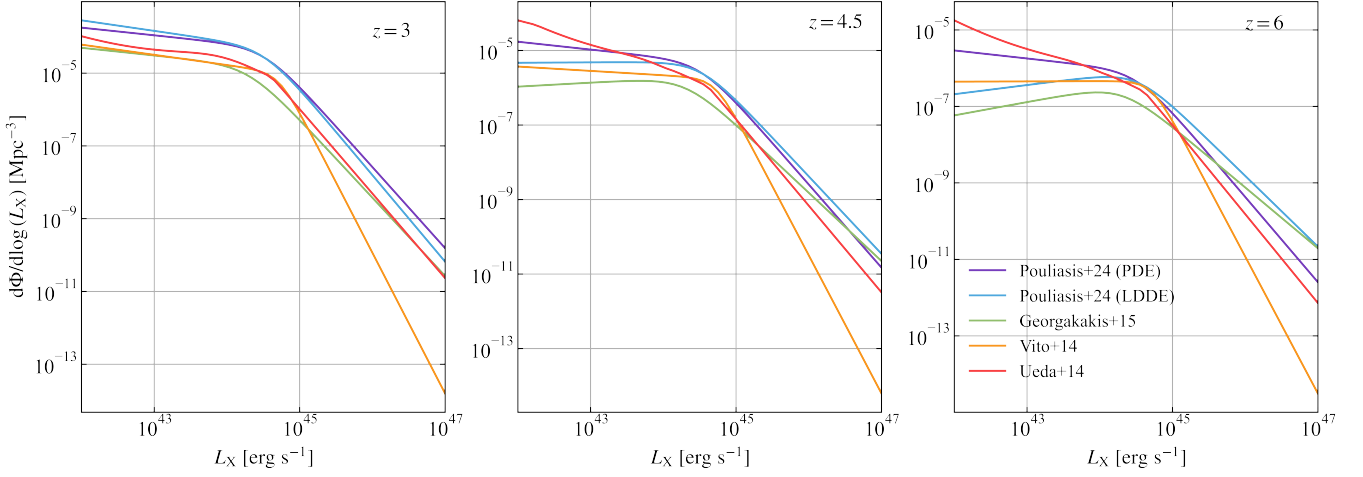


Figure 1. Comparison of the X-ray luminosity functions at $z = 3$ (left), $z = 4.5$ (middle) and $z = 6$ (right). We include the PDE and LDDE model from Pouliasis et al. (2024), the LDDE models from Georgakakis et al. (2015) and Vito et al. (2014), as well as a LDDE with a redshift cut-off from Ueda et al. (2014).

3 AGN NUMBER COUNT

For an AGN with X-ray luminosity L_X at redshift z , we also consider its hydrogen column density N_H , which quantifies how obscured the AGN is. Higher N_H values indicate significant obscuration, for example, due to absorption by a dusty torus or host-galaxy gases (Antonucci 1993; Netzer 2015). Compton-thick AGNs with $N_H > 10^{24} \text{cm}^{-2}$ can completely obscure soft X-ray emissions. Understanding N_H is essential for probing the physical properties of AGN environments and their impact on observed spectra (Elitzur & Shlosman 2006).

The number count of AGNs in a given comoving volume V can be written as (Vijarnwannaluk et al. 2022)

$$N = \iiint f_{\text{abs}}(\log L_X, z, N_H) \frac{d\Phi(\log L_X, z)}{d \log L_X} \times f_{\text{sky}} \frac{dV}{dz} d \log L_X dz d \log N_H, \quad (9)$$

where

$$\frac{dV}{dz} = \frac{4\pi}{H(z)} \left(\int_0^z \frac{dz'}{H(z')} \right)^2, \quad (10)$$

$$H(z) = H_0 \left[\Omega_m (1+z)^3 + \Omega_\Lambda \right]^{\frac{1}{2}}. \quad (11)$$

The absorption function f_{abs} depends on X-ray luminosity, redshift and N_H . We use the functional form of f_{abs} given in Ueda et al. (2003), and choose $f_{\text{sky}} = 54.8 \text{ deg}^2$, in agreement with the *S82-XL* survey.

4 EXTREME-VALUE MODELLING OF THE BRIGHTEST AGNS

4.1 Extreme-value statistics

Here we give an overview of how the EVS framework can be used to determine the luminosity of the brightest X-ray AGNs expected in a given volume.

We utilise the generalised extreme-value (GEV) method, also known as the block maxima method (Gumbel 1958; de Haan & Ferreira 2006). In this method, we divide the AGN population in a given redshift bin into N distinct blocks, from each of which we

identify the brightest AGN. Analogous to the Central Limit Theorem, in the large- N limit, the distribution of the brightest AGNs will approach the generalised extreme-value distribution (equation (14)).

The calculation pipeline is as follows. First, we calculate the number count of $N(> L_X)$ of AGNs with X-ray luminosity greater than L_X in a given redshift bin using equation (9). Next, we consider the probability P_0 that no AGNs in a given volume exceeds the maximum luminosity L_X . The probability distribution $P_0(L_X)$ can be modelled as a Poisson distribution with the following cumulative distribution function (cdf):

$$P_0(L_X) = \exp(-N(> L_X)), \quad (12)$$

Differentiating this with respect to L_X , we obtain the probability density function (pdf):

$$\frac{dP_0}{dL_X} = -\frac{dN(> L_X)}{dL_X} P_0(L_X), \quad (13)$$

The Fisher-Tippett-Gnedenko theorem implies that in the large- N limit, the cdf (equation (12)) approaches the GEV distribution given by:

$$G(L_X) = \begin{cases} \exp \left[-(1 + \gamma y)^{-1/\gamma} \right] & (\gamma \neq 0), \\ \exp [-e^{-y}] & (\gamma = 0), \end{cases} \quad (14)$$

where $y = (L_X - \alpha)/\beta$, with α describing the location of the peak, and β describing the scale of the pdf. The sign of the parameter γ determines the GEV type, with $\gamma = 0$, $\gamma > 0$ and $\gamma < 0$, corresponding to the Gumbel, Fréchet and Weibull distributions respectively.

We can express the GEV parameters α , β and γ in terms of astrophysical parameters by Taylor-expanding the Poisson distribution and GEV distribution around the peak of the pdf at L_X to cubic order. By equating coefficients, we find

$$\begin{aligned} \gamma &= N(> L_{\text{peak}}) - 1, \\ \beta &= \frac{(1 + \gamma)^{1+\gamma}}{\left. \frac{dN}{dL_X} \right|_{L_{\text{peak}}}}, \\ \alpha &= L_{\text{peak}} - \frac{\beta}{\gamma} \left((1 + \gamma)^{-\gamma} - 1 \right), \end{aligned} \quad (15)$$

In Fig. 2, we plot the extreme-value pdf for the brightest AGNs for three redshift bins $z = [3, 3.5]$, $[4.5, 5]$ and $[5, 5.5]$ where the distributions shown are calculated from equation (14). The values for

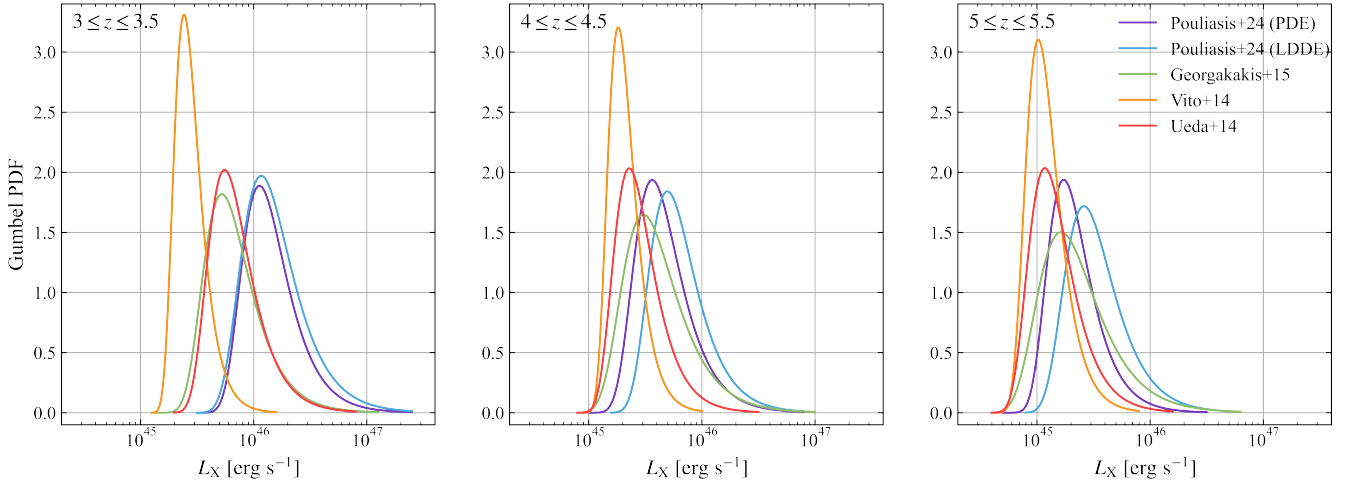


Figure 2. The probability density functions for the most luminous AGNs calculated in Section 2 for three redshift bins: $z = [3, 3.5]$ (left), $z = [4.5, 5]$ (middle) and $z = [5, 5.5]$ (right). These plots show the EVS pdf taken to be Gumbel, where we assume $\gamma = 0$. The values for α and β which describe the curves are given in Table A1.

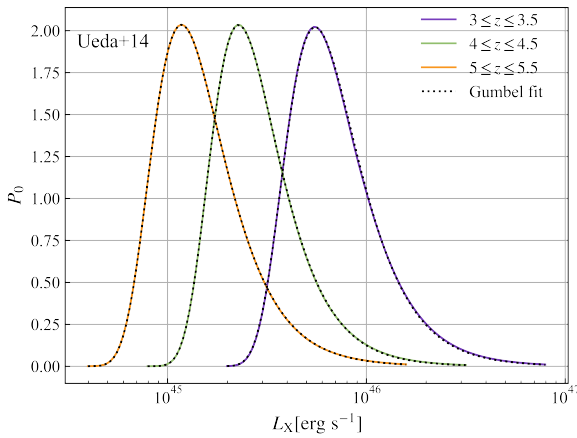


Figure 3. A plot to show the comparison of the Gumbel fit to the Poisson pdf with three redshift bins for the cut-off redshift LDDE luminosity function in Section 2.3. The solid coloured lines show the pdf derived from the Poisson distribution (equation 13) and the dashed lines are the Gumbel distribution (equation 14) with $\gamma = 0$ and the values for α and β given in Table A1. We can see that choosing the Gumbel distribution, where we take $\gamma = 0$, is a suitable fit for our data.

α and β , are calculated from equations 15 and shown in Table A1 in the Appendix. We note from the Table that α is indeed close to the peak luminosity in each redshift bin.

We found that for each of the luminosity functions, the value of γ is small ($\gamma \lesssim |0.05|$). Hence, the GEV distribution is well approximated by the Gumbel distribution ($\gamma = 0$). In Fig. 3, we give a visual comparison of the extreme-value pdf calculated from equation (13) to its Gumbel approximation, using the Ueda et al. (2014) model as an example.

From these figures, we see that as redshift increases, the peak extreme values of L_X decrease. We also see that different luminosity functions decrease at different rates. For example, the PDE model from Pouliaxis et al. (2024) decreases in luminosity at a higher rate than its LDDE variation.

Our next goal is to see whether any of these extreme-value pdfs are consistent with observation of the brightest X-ray AGNs.

4.2 *Stripe 82* X-ray AGN data

The *Stripe 82* X-ray survey is a comprehensive astronomical survey focused on detecting rare, high-luminosity AGNs and other X-ray sources within the area covered by the *Stripe 82* field of the Sloan Digital Sky Survey (SDSS). The survey incorporates data from the *XMM-Newton* and *Chandra* telescopes to create a comprehensive catalogue of X-ray sources (e.g. LaMassa et al. 2013, 2016). The continuous updates to the catalogue have been invaluable to the study of the high-redshift Universe.

We take data from the *S82X* catalogues as described in LaMassa et al. (2024) and Peca et al. (2024). These catalogues provide samples at $z \lesssim 3.5$ and $3 \lesssim z \lesssim 6$, with sky survey areas of $\sim 31.3 \text{ deg}^2$ and 54.8 deg^2 , respectively.

LaMassa et al. (2024) also gave the Eddington luminosity (L_{Edd}) for samples with $z \lesssim 3.5$, which was calculated using the reference black hole mass according to the formula

$$L_{\text{Edd}} = 1.26 \times 10^{38} M_{\text{BH}}/M_{\odot} \text{ erg s}^{-1}. \quad (16)$$

The 2–10 keV luminosity is used as a proxy for L_X . However, it has been suggested that statistical analyses of the black hole mass measurements should focus on masses derived from the same single-epoch emission-line formula. For example, discrepancies between black hole masses estimated using Balmer lines and the MgII line were found to be 0.27–0.42 dex, whereas even larger discrepancies of 0.43–0.58 dex were found when comparing black hole masses derived from the CIV line with those derived from the H α and H β lines (Shen et al. 2024). Due to these inconsistencies in black hole mass measurements, we opt to use only the publicly available L_{Edd} values from LaMassa et al. (2024) rather than calculating new values using reference black hole masses.

For the EVS analysis, we will use a subset of 35 AGNs from the *S82X* data. This is comprised of 17 sources from LaMassa et al. (2024) in the redshift range $3 \ll z \ll 6$ which were given values for the Eddington limit, plus the brightest 18 sources from Peca et al. (2024) in the range $3.5 \leq z \leq 6$.

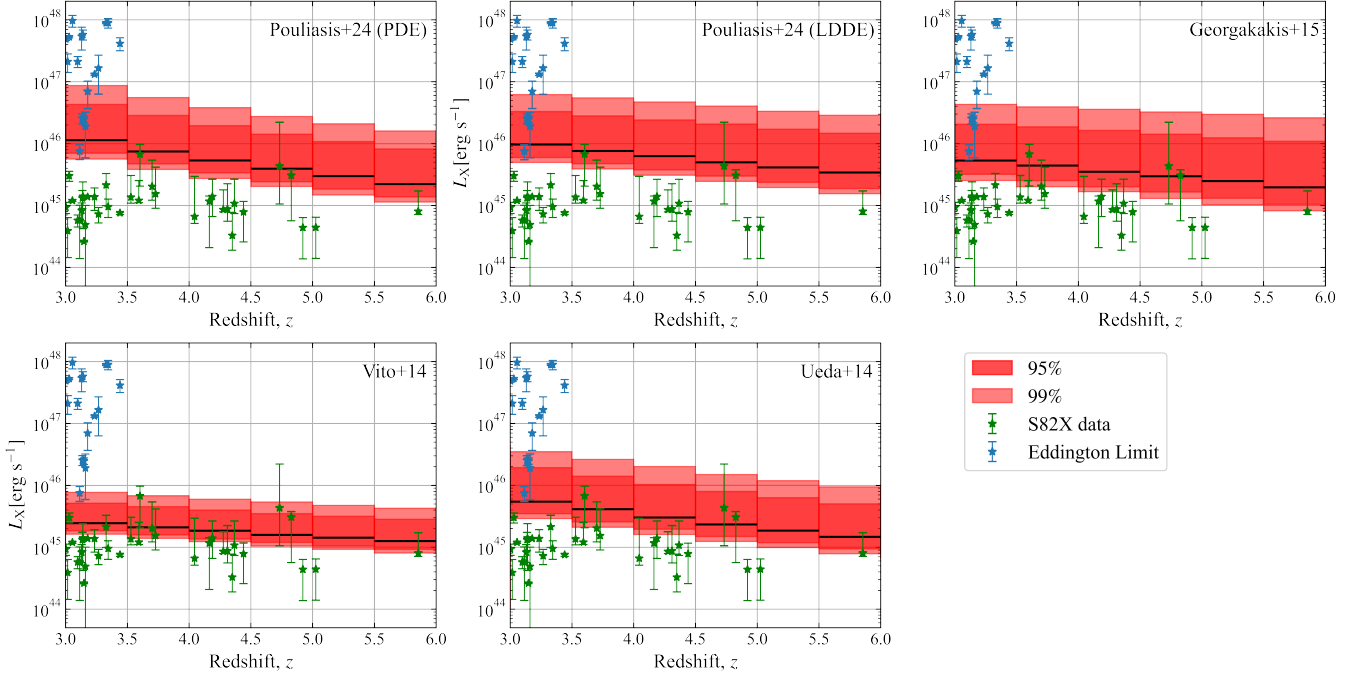


Figure 4. The peak luminosities of L_X (solid black lines) of the extreme-value (Gumbel) pdf for the L_X functions from Section 2, plotted in redshift bins of size 0.5 from $z = 3$ to $z = 6$. Each block shows a profile of the EVS probability density function shown in fig. 2 where the darker/ lighter shaded regions correspond to the 95th and 99th percentiles. The data points (in green) are from the S82-XL survey Peca et al. (2024), and the Eddington luminosities (blue) are from LaMassa et al. (2024).

5 RESULTS

The main result of this work is shown in Fig. 4. The figure shows the profile of the extreme-value pdfs (showing the peak values in black, plus the 95th and 99th percentile bands) across redshift bins in the range $3 \lesssim z \lesssim 6$, assuming five different luminosity functions discussed in Section 2. The step-like feature comes from the fact that we calculate a single EVS distribution in each redshift bin of width 0.5. We include data points from the S82X catalogue described in Section 4.2, and also show the Eddington limit for a selection of these AGN as reported in LaMassa et al. (2024).

Overall we see general consistency between the brightest S82X data and the EVS predictions, which are around 1-2 of magnitudes in L_X below the Eddington limits. We also note the following.

- We see three AGNs that seem to be in slight tension with the EVS predictions of extreme luminosities. These are 2CXO J001217.1-005437 and 2CXO J021043.1-001817 from Chandra, and 4XMM J000748.9+004119 from XMM-Newton, with redshifts $z \approx 3.60, 4.73, 4.83$. respectively. For certain luminosity functions (Georgakakis et al. (2015), Vito et al. (2014), Ueda et al. (2014)), these AGNs lie above the expected peak values.

- The Vito et al. (2014) model has the narrowest EVS bands, centering around lower values of L_X than other models (*i.e.* the values of the EVS parameters α and β in Table A1 are the smallest amongst the models). The brightest AGNs straddle the outer edges of this band, showing some tension. The hard X-ray AGN luminosity function in Vito et al. (2014) may be biased due to its calibration from soft-band X-ray AGN samples and assuming a simple power-law spectrum with photon index $\Gamma = 1.8$. This could explain the sharp drop in L_X at high luminosities in Fig. 1 in contrast with other luminosity functions.

- The Georgakakis et al. (2015) model has the broadest EVS

band, and share a similar shape with the Pouliasis et al. (2024) LDDE model. Their extreme luminosity values show a more gradual decline with redshift.

- The Pouliasis et al. (2024) (PDE) and the Ueda et al. (2014) models have similar profiles, with the PDE model predicting slightly higher values for extreme luminosity over the redshift range.
- The predicted upper limits of the EVS bands are in broad agreement with the Eddington limits in the range $z = 3 - 3.5$. This underscores the robustness of the Eddington threshold as a natural upper bound on AGN luminosities. Nevertheless, for the Pouliasis models, the Eddington luminosities fall within the *lower* estimates of extreme luminosities, hence showing more tension compared with other models.

6 DISCUSSION AND CONCLUSION

In summary, using the EVS formalism, we obtained the prediction for the extreme X-ray luminosities of AGNs in the redshift range $3 \lesssim z \lesssim 6$. We derived the probability distribution of extreme luminosities, which we found to be well approximated by the Gumbel distribution. Our main results are shown in Fig. 4 and 5, where we compare observational data with our EVS predictions assuming 5 different semi-analytic models of the luminosity functions. We find good agreement between the models and data, with the Vito model showing most tension with data. The upper end of the extreme luminosities are also found to be generally consistent with Eddington luminosities, but arguably in some tension with the Pouliasis models.

Further discussion points are as follows.

- *At lower redshifts:* Elías-Chávez et al. (2024) analyzed the X-ray properties of 23 brightest AGNs from the XMM-Newton Ultra Narrow Deep Field survey, with redshifts up to 2.66. Their 2–10 keV

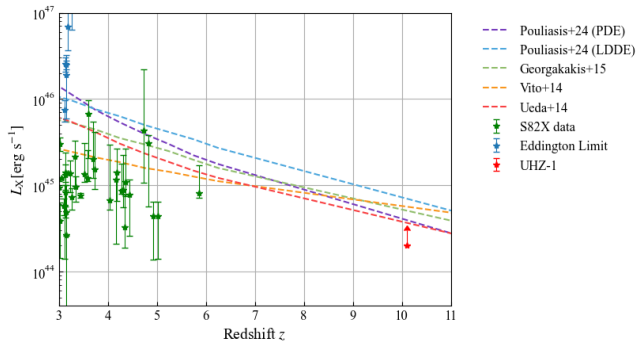


Figure 5. A comparison of EVS predictions for various luminosity functions from Section 2, extended to redshift $z = 11$. We include data points from S82-XL for $z > 3$, as well as UHZ-1 (Goulding et al. 2023) at redshift $z = 10.1$. Each dashed line shows the peak of the extreme-value pdf for each luminosity function (percentile bands not shown).

luminosity was found to be $L_X \sim 10^{42} - 10^{46} \text{ erg s}^{-1}$. Despite ranking among the most luminous AGNs observed in X-ray surveys to date, their luminosities are still consistent with the EVS predictions for all luminosity functions investigated here when extrapolated at the lower end.

- *At higher redshifts:* We can extend the EVS modelling to estimate the extreme X-ray luminosities of AGNs at, say, $z \sim 10$ where an AGN observation has been made (Goulding et al. 2023).

In Fig. 5, we plot the peak values of the extreme-value pdf, smoothed over redshifts, extended to $z = 11$. These lines correspond to the smoothed version of each model shown in Fig. 4 up to $z = 6$. We see that at $z \sim 10$, the peak of the EVS distribution is around $10^{44} - 10^{45} \text{ erg s}^{-1}$ for all models considered in this paper.

We also include an additional data point, UHZ-1, from Goulding et al. (2023), which has been spectroscopically confirmed at $z = 10.1$ with $L_X \gtrsim 2 \times 10^{44} \text{ erg s}^{-1}$. Its luminosity is in agreement with the EVS prediction from various luminosity functions.

- *Future direction:* The luminosity functions we used have not been calibrated to these higher redshifts, where a more comprehensive semi-analytic model is needed along with more observational data. Habouzit et al. (2022) compared AGN populations across various large-scale hydrodynamical simulations and found significant discrepancies in AGN luminosity functions, especially at high redshifts. These inconsistencies reveal key challenges in our understanding of AGN feedback, obscuration patterns, duty cycle and accretion processes in the very early Universe. Future X-ray telescopes such as Athena¹, AXIS², and LynX³ will refine these models through their enhanced sensitivity, enabling detection of faint AGNs at unprecedented redshifts and providing new insights into AGN obscuration and evolution (e.g. Schirra et al. 2021).

ACKNOWLEDGEMENTS

C.H. is supported by the Warwick Mathematics Institute Centre for Doctoral Training, and gratefully acknowledges funding from the University of Warwick and the UK Engineering and Physical Sciences Research Council (grant number: EP/W524645/1). P.C. ac-

knowledges support from (i) Suranaree University of Technology (SUT), (ii) Thailand Science Research and Innovation (TSRI), and (iii) National Science, Research and Innovation Fund (grant number 204265).

DATA AVAILABILITY

The data used in this article will be shared on reasonable request to the corresponding author.

REFERENCES

- Aird J., Coil A. L., Georgakakis A., Nandra K., Barro G., Pérez-González P. G., 2015, *MNRAS*, **451**, 1892
- Antonucci R., 1993, *ARA&A*, **31**, 473
- Booth C. M., Schaye J., 2009, *MNRAS*, **398**, 53
- Chantavat T., Chongchitnan S., Silk J., 2023, *MNRAS*, **522**, 3256
- Chongchitnan S., Silk J., 2012, *Phys. Rev. D*, **85**, 063508
- Chongchitnan S., Silk J., 2021, *Phys. Rev. D*, **104**, 083018
- Chongchitnan S., Chantavat T., Zunder J., 2021, *Astronomische Nachrichten*, **342**, 648
- Elías-Chávez M., et al., 2024, *MNRAS*, **532**, 1564
- Elitzur M., Shlosman I., 2006, *ApJ*, **648**, L101
- Fabian A. C., 2012, *ARA&A*, **50**, 455
- Fabian A. C., Lohfink A., Kara E., Parker M. L., Vasudevan R., Reynolds C. S., 2015, *MNRAS*, **451**, 4375
- Fabjan D., Borgani S., Tornatore L., Saro A., Murante G., Dolag K., 2010, *MNRAS*, **401**, 1670
- Georgakakis A., et al., 2015, *MNRAS*, **453**, 1946
- Goulding A. D., et al., 2023, *ApJ*, **955**, L24
- Gumbel E. J., 1958, *Statistics of extremes*. Columbia university press
- Habouzit M., et al., 2022, *MNRAS*, **509**, 3015
- Hasinger G., 1998, *Astronomische Nachrichten*, **319**, 37
- Heather C., Chantavat T., Chongchitnan S., Silk J., 2024, *MNRAS*, **534**, 173
- Inayoshi K., Visbal E., Haiman Z., 2020, *ARA&A*, **58**, 27
- Kormendy J., Ho L. C., 2013, *ARA&A*, **51**, 511
- LaMassa S. M., et al., 2013, *MNRAS*, **436**, 3581
- LaMassa S. M., et al., 2016, *ApJ*, **817**, 172
- LaMassa S., et al., 2024, *ApJ*, **974**, 235
- Maccacaro T., Gioia I. M., Avni Y., Giommi P., Griffiths R. E., Liebert J., Stocke J., Danziger J., 1983, *ApJ*, **266**, L73
- Maccacaro T., della Ceca R., Gioia I. M., Morris S. L., Stocke J. T., Wolter A., 1991, *ApJ*, **374**, 117
- Miyaji T., Hasinger G., Schmidt M., 2000, *A&A*, **353**, 25
- Mushotzky R. F., Done C., Pounds K. A., 1993, *ARA&A*, **31**, 717
- Netzer H., 2015, *ARA&A*, **53**, 365
- Peca A., et al., 2024, *ApJ*, **974**, 156
- Pouliaxis E., et al., 2024, *A&A*, **685**, A97
- Pozdnyakov L. A., Sobol I. M., Sunyaev R. A., 1983, *Astrophysics Space Physics Research*, **2**, 189
- Rees M. J., 1984, *ARA&A*, **22**, 471
- Rybicki G. B., Lightman A. P., 1986, *Radiative Processes in Astrophysics*
- Schirra A. P., et al., 2021, *MNRAS*, **508**, 4816
- Shen Y., et al., 2024, *ApJS*, **272**, 26
- Sijacki D., Springel V., Di Matteo T., Hernquist L., 2007, *MNRAS*, **380**, 877
- Stanley F., et al., 2017, *MNRAS*, **472**, 2221
- Ueda Y., Akiyama M., Ohta K., Miyaji T., 2003, *ApJ*, **598**, 886
- Ueda Y., Akiyama M., Hasinger G., Miyaji T., Watson M. G., 2014, *ApJ*, **786**, 104
- Veronesi N., Rossi E. M., van Velzen S., 2023, *MNRAS*, **526**, 6031
- Vijarnwannaluk B., et al., 2022, *ApJ*, **941**, 97
- Vito F., Gilli R., Vignali C., Comastri A., Brusa M., Cappelluti N., Iwasawa K., 2014, *MNRAS*, **445**, 3557
- Yuan F., Narayan R., 2014, *ARA&A*, **52**, 529

¹ <https://www.the-athena-x-ray-observatory.eu>

² <https://axis.umd.edu>

³ <https://www.lynxobservatory.com>

de Haan L., Ferreira A., 2006, Extreme Value Theory: an introduction.
Springer, New York

APPENDIX A:

Table A1 shows the peak luminosities and GEV parameters (α and β) for the various luminosity functions used in each redshift bin, to four significant figures. The parameters have been calculated using equation (15) assuming $\gamma = 0$, in other words assuming the Gumbel distribution.

This paper has been typeset from a \TeX/L\AA\TeX file prepared by the author.

X-ray luminosity function	Redshift	Peak L_X	α	β
Pouliasis et al. (2024) (PDE)	$3 \leq z \leq 3.5$	46.06	46.05	0.1950
	$3.5 \leq z \leq 4$	45.87	45.88	0.1929
	$4 \leq z \leq 4.5$	45.73	45.73	0.1902
	$4.5 \leq z \leq 5$	45.59	45.59	0.1894
	$5 \leq z \leq 5.5$	45.48	45.47	0.1899
	$5.5 \leq z \leq 6$	45.35	45.35	0.1902
Pouliasis et al. (2024) (LDDE)	$3 \leq z \leq 3.5$	45.98	45.98	0.1870
	$3.5 \leq z \leq 4$	45.88	45.89	0.1934
	$4 \leq z \leq 4.5$	45.80	45.80	0.2002
	$4.5 \leq z \leq 5$	45.70	45.70	0.2075
	$5 \leq z \leq 5.5$	45.62	45.61	0.2149
	$5.5 \leq z \leq 6$	45.53	45.52	0.2231
Georgakakis et al. (2015)	$3 \leq z \leq 3.5$	45.78	45.79	0.1924
	$3.5 \leq z \leq 4$	45.73	45.72	0.2024
	$4 \leq z \leq 4.5$	45.65	45.64	0.2128
	$4.5 \leq z \leq 5$	45.55	45.55	0.2235
	$5 \leq z \leq 5.5$	45.47	45.47	0.2340
	$5.5 \leq z \leq 6$	45.39	45.38	0.2454
Vito et al. (2014)	$3 \leq z \leq 3.5$	45.34	45.38	0.1111
	$3.5 \leq z \leq 4$	45.32	45.32	0.1128
	$4 \leq z \leq 4.5$	45.27	45.26	0.1149
	$4.5 \leq z \leq 5$	45.20	45.20	0.1166
	$5 \leq z \leq 5.5$	45.16	45.15	0.1187
	$5.5 \leq z \leq 6$	45.10	45.10	0.1206
Ueda et al. (2014)	$3 \leq z \leq 3.5$	45.74	45.74	0.1824
	$3.5 \leq z \leq 4$	45.62	45.61	0.1815
	$4 \leq z \leq 4.5$	45.48	45.49	0.1811
	$4.5 \leq z \leq 5$	45.37	45.37	0.1811
	$5 \leq z \leq 5.5$	45.27	45.27	0.1811
	$5.5 \leq z \leq 6$	45.17	45.17	0.1814

Table A1. The peak X-ray Luminosity, L_X , and the Gumbel parameters α and β for the luminosity functions described in Section 2.